Biomechanical performances of PCL/HA micro- and macro-porous lattice scaffolds fabricated via laser powder bed fusion for bone tissue engineering

**Biomechanical performances of PCL/HA micro- and macro-porous lattice scaffolds fabricated via laser powder bed fusion for bone tissue engineering**

Maria Laura Gatto[1*], Michele Furlani[2], Alessandra Giuliani[2], Nora Bloise[3,4], Lorenzo Fassina[5], Livia Visai[3,4], Paolo Mengucci[1]

[1] *Department of Materials, Environmental Sciences and Urban Planning, Polytechnic University of Marche, Via Brecce Bianche, 60131 Ancona, Italy*

[2]*Department of Clinical Science, Polytechnic University of Marche, Via Brecce Bianche, 60131 Ancona, Italy*

[3] *Department of Molecular Medicine, Centre for Health Technologies (CHT), INSTM UdR of Pavia, University of Pavia, 27100 Pavia, Italy*

[4] *Medicina Clinica-Specialistica, UOR5 Laboratorio di Nanotecnologie, ICS Maugeri, IRCCS, Pavia, Italy*

[5]*Department of Electrical, Computer and Biomedical Engineering, Centre for Health Technologies (CHT), University of Pavia, Via Ferrata 5, 27100 Pavia, Italy*

***Corresponding author:**

Maria Laura Gatto
Dipartimento SIMAU
Università Politecnica delle Marche
Via Brecce Bianche 12
60131 Ancona
Italy

Phone: +39 071 2204751
E-mail: m.l.gatto@pm.univpm.it

**ABSTRACT**

The present experimental study aims to extend know-how on resorbable polycaprolactone/hydroxyapatite (PCL/HA, 70/30 wt.%) scaffolds, produced by Laser Powder Bed Fusion (LPBF) technology, to geometrically complex lattice structures and micro porous struts. Using optimized LPBF printing parameters, micro- and macro-porous scaffolds for bone tissue regeneration were produced by regularly repeating in space Diamond (DO) and Rhombic Dodecahedron (RD) elementary unit cells. After production, scaffolds were submitted to structural, mechanical, and biological characterization. The interaction of scaffolds with human Mesenchymal Stem Cells (hMSCs) allowed studying the degradative processes of the PCL matrix. Biomechanical performances and biodegradation of scaffolds were compared to literature results and bone tissue data. Mechanical compression test, biological viability up to 4 days of incubation and degradation rate evidenced strong dependence of scaffold behavior on unit cell geometry as well as on global geometrical features.

**KEYWORDS**

Polycaprolactone/hydroxyapatite scaffold; laser powder bed fusion; unit cell topology; tissue engineering; mechanical properties; mesenchymal stem cells.

## 1. INTRODUCTION

Biodegradable scaffolds act as temporary tissue substitutes, providing mechanical support and biological activities during tissue regeneration [1,2]. A wide range of natural and synthetic biodegradable polymers are commonly used in biomedical applications due to superior ability in design customization and chemical modification [3]. Temporary matrices of thermoplastic aliphatic polyesters such as PolyLactic Acid (PLA), PolyGlycolic Acid (PGA), PolyLactide-co-Glycolide Acid (PLGA) and PolyCaproLactone (PCL) [4], encourage bone tissue regeneration, providing structural support without damaging the biological tissue [5].

High potential production technology of polymer-based scaffolds for bone tissue regeneration was identified in Additive Manufacturing (AM) [6,7]. Among the various AM technologies available to produce polymeric scaffolds, Laser Powder Bed Fusion (LPBF) and Material Extrusion (ME) have received particular attention, given their suitability for industrial needs. ME allows for a low level of complexity and is fast and cheap. On the other hand, LPBF provides high dimensional accuracy of parts, with reduced total costs in case of multiple batches [8]. The limited resolution of ME is inherent in the technological process due to the nozzle size used to extrude the heated polymer filament, and the precision of the nozzle movement in the XY plane. Furthermore, misalignment of layers as well as deformation and shrinkage of extruded parts compromise accuracy and surface smoothness of the final component [8]. Resolution of parts produced by the LPBF technology mainly depends on the spot size of laser used to melt powder on the building platform [8]. Therefore, optimization of the printing parameters in the LPBF process allows to improve the dimensional accuracy of parts, thus enabling the production of polymer-based scaffolds with micro- and macro-porous geometry, which meet the requirements for bone regeneration. The main advantages of using the LPBF technique to produce micro- and macro-porous scaffold are consistency and reproducibility of complex structures [9].

Different combinations of laser power, scan speed, scan spacing and temperature of the powder bed are proposed in literature to successfully produce bulk samples based on hydroxyapatite (HA) - reinforced polycaprolactone (PCL) [10-14] by the LPBF technology and for obtain polymeric scaffolds with micro-porous struts [9]. While, the CAD design of the elementary unit cell geometry defines the scaffold macro-porosity, the printing parameters used in the LPBF process totally determine the micro-porosity of the scaffold [9].

Regarding scaffold macro-porosity, recent simulation studies on unit cell topology [15,16] concluded that midline-symmetrical elementary unit cell geometry, such as Rhombic Dodecahedron (RD), is suitable for load-bearing implants that support the body weight directly, with high mass transfer performance. On the other hand, diagonal-symmetrical elementary unit cell, such as Diamond (DO),

has been proposed as the best choice for implants that require large torsional forces, with advantages on implant fixation, cell growth environment and tissue regeneration [15,16]. The appropriate design of elementary unit cell topology allows controlling strut thickness, which determines the size of macro-pores (> 100 µm) [9], which in turn influences both mechanical and biological performances. On the other hand, small pores (40 - 100 µm) inside struts constitute the scaffold micro-porosity [9] which increases the specific surface of the material, thus improving permeability, enhancing scaffold degradation and increasing the number of sites available for protein absorption, that improve cells adhesion, proliferation, differentiation and mineralization [17-19].

PCL is a cheap FDA-approved semi-crystalline polymer for load-bearing applications, with high thermal stability, low degradation rate and low biocompatibility due to the marked hydrophobicity. To overcome this latter limiting issue, association of PCL and HA was proposed [20,21]. HA shows excellent bioactivity and osteoconductivity properties, although it is brittle, with poor tensile properties [22]. Therefore, the combination of PCL and HA meets biological and mechanical requests for scaffold applications in bone tissue regeneration [23]. Systematic studies in the literature have demonstrated that the quantity of HA capable of enhancing both cell proliferation and mechanical behavior of PCL/HA mixture is about 30 wt.% [11]. Despite the large number of papers dealing with this topic, studies combining LPBF and PCL/HA (30 wt.%) for scaffold production in perspective of bone tissue regeneration have limited to investigate very simple scaffold geometries, such as solid discs with porous network due to spaces between particles [14], cubic reticular structures [10-12] and cylinders with orthogonal square channels [13].

This experimental study aims to fill the gap between complexity of unit cell topology and biomechanical performances of PCL/HA micro- and macro-porous scaffolds for bone tissue regeneration, thus extending the know-how to geometrically complex structures formed of single elementary unit cell regularly repeated in space. In this work, PCL/HA (30 wt.%) micro- and macro-porous scaffolds with DO and RD elementary unit cells geometry produced by the LPBF technology were submitted to structural, mechanical, biological, and matrix-cells interaction characterization.

Scaffold performances were compared to previous literature results and native bone data. Short-term viability tests up to 4 days were carried out to have a fast check of scaffold biological response, as already validated for Ti-based scaffolds [24]. Mechanical and biological tests provided useful indication on scaffold design in view of efficient implant osseointegration.

## 2. MATERIALS AND METHODS

### *2.1 Design and production*

Two different scaffold architectures (Figure 1) were created by repeating Diamond (DO) and Rhombic Dodecahedron (RD) elementary unit cells, 1 mm edge size (Figure 1A and Figure 1B, respectively) to fill $10\times10\times10$ $mm^3$.

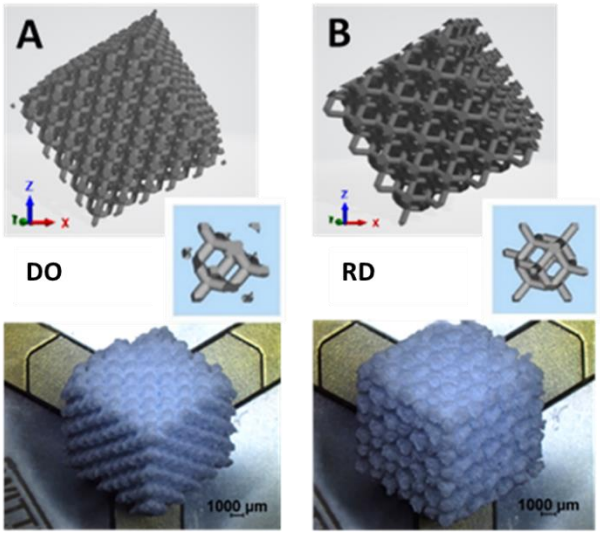


**Figure 1** Schematics of scaffold geometries: (A) Diamond (DO) and (B) Rhombic Dodecahedron (RD) elementary unit cells.

Nominal values of porosity and strut size of DO and RD scaffolds obtained from the CAD data are reported in Table 1.

**Table1** Nominal values of porosity and strut size for DO and RD geometries from CAD data

| Geometry | Porosity (%) | Strut size (mm) |
|---|---|---|
| **DO** | 80 | 0.42 |
| **RD** | 80 | 0.46 |

Powder mixture containing 70 wt.% polycaprolactone (PCL, Eurocoating S.p.a.) and 30 wt.% hydroxyapatite (HA, Boc Sciences, Inc., Shirley, NY, USA) was used to manufacture scaffolds by the Laser Powder Bed Fusion (LPBF) technology, using an EOS P770 system (EOS GmbH, Munich, Germany). Scaffolds were produced with intrinsic micro-porosity in the struts, using the machining parameters reported in Table 2, optimized according to Eshraghi et al. [13]. After manufacturing, scaffolds were cleaned by air jetting followed by low pressure water jetting.

**Table 2** Values of the machining parameters used for scaffold production by the EOS 770 system.

| Parameter | Value |
|---|---|
| **Laser power (W)** | 1.2 |
| **Scan speed (mm/s)** | 914 |
| **Scan spacing (µm)** | 150 |
| **Bed temperature (°C)** | 50 |

*2.2 Structural and morphological characterization*

*2.2.1 SEM and EDS analysis*

Scanning electron microscope (SEM) observations by Tescan Vega 3 (Tescan Company, Brno, Czech Republic) equipped with an EDAX Elements microanalysis (EDS) system were employed to observe the PCL/HA raw powder morphology, the surface and inner structure of scaffolds cut at half height (5 mm) and the adhesion of mesenchymal stem cells on the scaffold surface.

The chemical composition of raw powder and scaffolds was determined by EDS microanalysis. Results were obtained by averaging data taken from five different sample areas observed at the same magnification (500×). Chemical concentration of calcium (Ca), phosphorus (P) and the Ca/P ratio were considered.

*2.2.2 XRD*

Structural information from raw powder and scaffolds were achieved from X-ray diffraction (XRD), by using a Bruker D8 Advance diffractometer (Bruker, Karlsruhe, Germany) operating at V = 40 kV and I = 40 mA, with Cu-Kα radiation, in the angular range 2θ = 10° - 60°. Pattern analysis was performed by the DIFFRAC.EVA software package (Bruker), while XRD peaks shape analysis was conducted by the OriginPro software vers. 8.5 (OriginLab, Northampton, MA, USA).

*2.2.3 DSC*

Differential scanning calorimetry (DSC) measurements were performed on raw powders of PCL and HA separately, to investigate the different contribution of the compounds, using a PerkinElmer system (PerkinElmer, Waltham, MA, USA) in the temperature range 15 - 120 °C, at constant heating rate of 3 °C/min.

*2.2.4 Scaffold porosity*

Scaffold porosity P (%) was evaluated according to the following equation (1):

$$P = \left(V_{nom} - V_{eff}\right) * 100 \qquad (1)$$

where $V_{nom}$ = 1 $cm^3$ is the nominal scaffold volume and $V_{eff} = \frac{W}{\rho_{mat}}$ is the effective manufactured scaffold volume, defined as the ratio between scaffold weight (W) and material density ($\rho_{mat}$). As

reference value of the material density was assumed $\rho_{mat}$=1.76 g/cm$^3$, calculated on the basis of weight percentage and density of compounds: 70 wt.% PCL ($\rho_{PCL}$=1.15 g/cm$^3$), 30 wt.% HA ($\rho_{HA}$=3.18 g/cm$^3$). From the porosity value P, the relative density $\rho = 1 - \frac{P}{100}$ was estimated [16]. Density of struts ($\rho_s$) was quantified as [16] $\rho_s = \rho * \rho_{mat}$. This latter parameter estimates the total density of scaffold without porosity, allowing to compare the porous scaffold structure to the bulk structure of bone.

*2.2.5 XμCT*

X-ray computed microtomography (XμCT) analysis was performed by a Bruker Skyscan 1174 system (Bruker, Kontich, Belgium), to quantify the scaffolds morphometric parameters. Projections were obtained with V = 50 kV, I = 800 μA and the following experimental settings:

- pixel size = 13.8 μm;
- total rotation angle = 180°;
- rotation step = 0.2°;
- projection exposure time = 4 s;
- aluminum (Al) energy filter = 0.25 mm.

Projections were processed in stacks of cross-sectional slices by the SkyScan reconstruction program NRecon (vers. 1.10.6.2, Bruker), under the following conditions:

- smoothing = 4;
- ring artefacts reduction = 2;
- beam hardening correction = 13%.

3D reconstructions of DO and RD scaffolds were performed by the Bruker SkyScan CT-vox software (vers. 3.3.0), and therefore related to information from 2D slices. DO and RD scaffold geometries were analyzed by the Bruker SkyScan CT-analyzer software (vers. 1.17.7.2). Four morphometric

parameters were estimated for both DO and RD geometries: a) average strut thickness (mm), b) average micro-pore size (mm), c) average macro-pore size (mm) and scaffold micro-porosity (%).

*2.2.6 PhC-XμCT*

Phase-contrast X-ray microtomography (PhC-XμCT) was carried out at the SYRMEP beamline of the ELETTRA Synchrotron Radiation facility (Trieste, Italy). Analysis was performed on scaffolds after 24 hours and 4 days of cells incubation in the culture medium, to investigate the interaction between hMSCs and scaffold material.

The approach used for the PhC-XμCT measurements is different from the XμCT analysis employed to quantify scaffold morphometric parameters. In conventional XμCT the imaging information is based on absorption contrast, while in the synchrotron phase-contrast setting, imaging is based on phase variation of the X-ray electromagnetic wave after interaction with the sample. For X-rays the refractive index n of the material is a complex number.

$$n = 1 - \delta + i\beta \quad (2)$$

In equation (2), $\delta$ is the decrement of the real part of the complex refractive index n, while the imaginary part $\beta$ is the extinction coefficient, which describes the material absorption. For common tissues and cells used in biological experiments, $\delta$ is about three order of magnitude greater than $\beta$, thus resulting in higher sensitivity of the phase-contrast approach respect to absorption contrast.

Experimental conditions, finely tuned to optimize discrimination of PCL, HA, and background, included: white X-ray beam with 19 keV peak energy; sample-to-detector distance of 10 cm and pixel size of 0.9 μm. Number of total projections for each sample was 2048, while the analyzed field of view (FOV) was $2048 \times 2048$ px$^2$, corresponding to an analyzed volume of about 6.3 mm$^3$, which is a small portion of the entire scaffold volume. However, considering the average strut thickness and pore size, as obtained from CAD design (Table 1), it can be argued that the analyzed FOV contains both material and voids. Tomographic slices reconstruction was carried out using the custom developed SYRMEP Tomo Project (STP) open source software [25], applying the Paganin's method

for phase retrieval algorithm [26]. Ten cubic volumes of interest (VOI) with voxel edge of 270 μm, were selected for each sample by ImageJ [27] and analyzed by VG Studio MAX 1.2 software (Volume Graphics GmbH, Heidelberg, Germany). Representative threshold values were manually set for PCL and HA, while structural analysis was carried out on three-dimensional images. Structural analysis allows to quantify: a) volume fraction (vol.%) of HA at scaffold nodes and in the struts forming the macro pores, after 24 hours cell culture, b) specific surface of the material close to the macro pores after 24 hours and 4 days cell culture ($\mu m^{-1}$).

2.3 *Roughness*

Roughness measurements were performed on scaffold surface by using a Nikon LV 150 Confovis Microscope (Nikon, Tokyo, Japan). Quantitative information was obtained from roughness maps via Nikon proprietary software, according to ISO 25178–603 [28].

*2.4 Mechanical tests*

Four different samples for each scaffold geometry were submitted to compressive tests using an Instron 5567 machine (Instron, Norwood, Massachusetts, USA) (5 kN, 0.5 mm/min). Due to the non-homogeneous structure of scaffold, the compressive stress was evaluated by averaging maximum applied load on effective scaffold area of load application. Values of the effective area for DO (92 $mm^2$) and RD (81 $mm^2$) geometries were obtained from the first five XμCT slices by the ROI Manager (Region of Interest Manager) analysis tool of ImageJ (ImageJ 1.52v, National Institutes of Health, Bethesda, Maryland, USA). Results were plotted as applied load (N) vs compression on initial sample height (%). In addition, compressive modulus was calculated from stress/strain curve according to ASTM D 1621e10 [29].

*2.5 Biological tests*

*2.5.1 Cell culture*

Human bone marrow mesenchymal stem cells (hBM-MSCs) were isolated and phenotypically analyzed to assess their mesenchymal properties according to the International Society for Cellular Therapy, as previously described [30,31]. The study protocols were approved by the Institutional Review Board of the Fondazione IRCCS Policlinico San Matteo and the University of Pavia (2011). Written informed consent was obtained from all the participants enrolled in this study. Cells used in all experiments were mainly at passage 4-5. hBM-MSCs were cultured at 37°C in a humidified incubator with 5% $CO_2$ in maintenance medium, low-glucose DMEM (Dulbecco's modified Eagle's medium) supplemented with 10% Mesencult, 2% glutamine, 1% penicillin-streptomycin (P-S) and 1% amphotericin B (Lonza Group Ltd.).

Before cell seeding, scaffolds were sterilized by 70% ethanol bath for 20 min, washed several times by sterilized water followed by PBS 1X and finally dried under UV exposure for 40 min. Afterwards, hMSCs ($5\times10^4$) were seeded on the control (Tissue Culture Polystyrene plate, TCPS) and onto each scaffold (previously placed in 24-well ultralow cell attachment plate, Corning, Inc., Corning, NY).

*2.5.2 Cell viability assay*

Resazurin-based assay (TOX8-1KT, Sigma-Aldrich) was performed to assess cell viability on both scaffold geometries (DO and RD) at 24 hours and 4 days from cell seeding. According to manufacturer instructions, resazurin solution was added in 1:10 ratio with respect to culture volume to each well plate and incubated for 4 h at 37 °C in 5% CO2. At the end of incubation time, absorbance of the samples was measured at a wavelength of 600 nm with a reference wavelength of 690 nm using a microplate reader (Bio-Rad Laboratories, Hercules, CA, USA). The cell viability assay was performed in parallel both on unseeded-scaffolds and on seeded-TCPS. Each biological experiment was performed in triplicate and in at least three separate tests. A standard curve of cell viability was used to express the results as percentage viable cells in comparison with TCPS. Results were expressed as mean value ± standard deviation. Statistical analysis of hMSC viability data after 24 hours and 4 days of incubation was carried out using GraphPad Prism 6.0 (GraphPad Inc., San Diego,

CA, USA) software package. Since two-way ANOVA analysis did not provide any significant result, Student's t-test was performed to determine statistical significance (significance levels: * $p \leq 0.05$ and ** $p \leq 0.01$).

### *2.5.3 Cell morphology*

After 24 hours and 4 days, hMSCs seeded scaffolds were processed in order to analyze cell morphology by SEM. Samples were fixed with 2.5% (v/v) glutaraldehyde solution in 0.1 M Na-cacodylate buffer (pH = 7.2) for 1 h at 4°C, washed with Na-cacodylate buffer, and then dehydrated at room temperature in an ethanol gradient series up to 100%. Samples were then lyophilized 6 h for complete dehydration and then sputter-coated with gold for SEM observations.

## 3. RESULTS

### *3.1 Powder characterization*

SEM images of raw powder (70 wt.% PCL, 30 wt.% HA) taken with backscattered electrons (BSE) are reported in Figure 2. In Figure 2A, PCL and HA particles are easily distinguishable by shape and contrast. PCL particles appear as irregular flakes with size ranging from 20 μm to 200 μm. On the contrary, HA particles are in brighter contrast, with globular shape and size in the range 5 – 30 μm (Figure 2B).

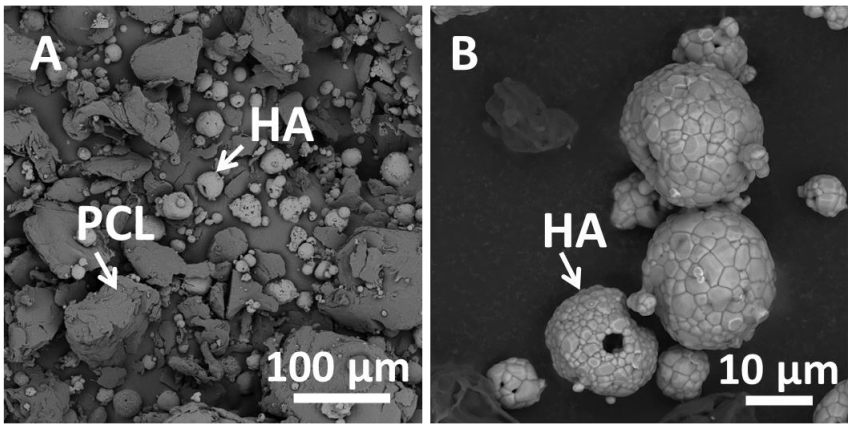


**Figure 2** SEM images of PCL/HA raw powder (A) and detail of HA particles (B).

Chemical composition analysis of raw powder, obtained by EDS, provided the following values of the main components of HA: Ca=2.7±0.3 (at.%) and P=1.22±0.13 (at.%) with atomic ratio Ca/P≈2.2±0.5.

XRD pattern of PCL/HA raw powder, in the full angular range investigated, is reported in Figure 3. Peak position of PCL is indicated by full dots while all remaining peaks are due to hydroxyapatite $Ca_{10}(PO_4)_6(OH)_2$, hexagonal, with lattice parameters a=0.93944 nm and c=0.68751 nm (ICDD 74-565). From Figure 3, in the mixed raw powder both PCL and HA are well crystallized.

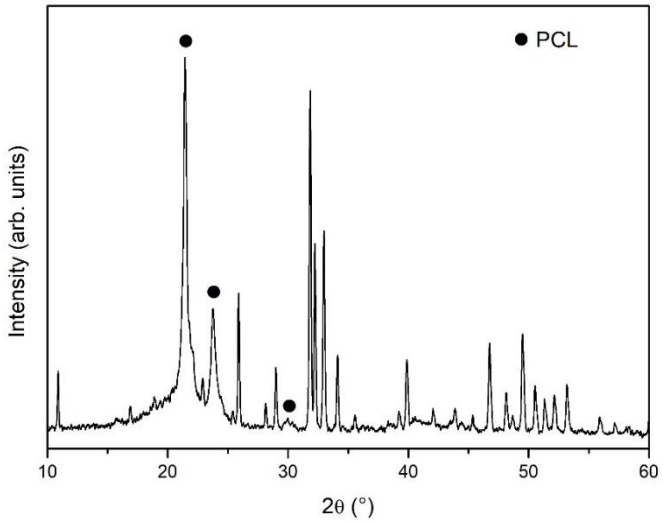


**Figure 3** XRD pattern of the mixed raw powder. PCL - full dot. All other peaks are due to HA.

DSC results for both PCL (solid line) and HA (dotted line) powders are shown in thermograms of Figure 4. PCL melts at about 70°C as evidenced by the endothermic effect. Broadening of the endo peak is due to the variability of PCL molecular weight, that causes melting of PCL particles over a fairly wide temperature range. On the contrary, HA powder provides a flat curve, indicating absence of any thermal effect in the investigated temperature range.

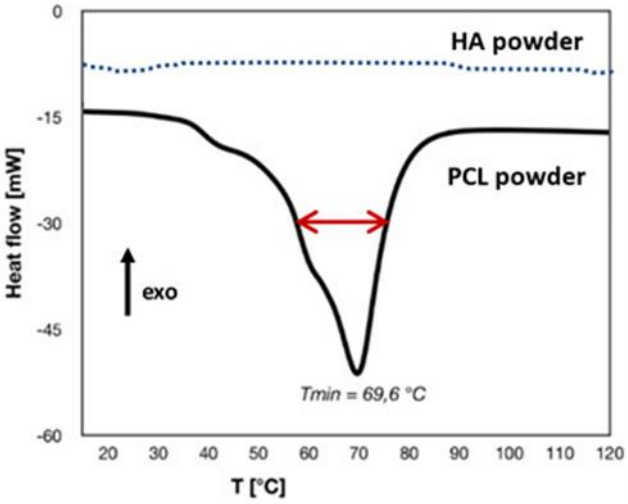


**Figure 4** DSC thermogram of PCL (continuous line) and HA (dashed line) powders.

*3.2 Scaffold characterization*

*3.2.1 SEM and EDS analysis*

SEM images of scaffolds top surface are reported in Figure 5 for both DO (Figure 5A) and RD (Figure 5B) geometries. Powder particles remain partially unmelted on the scaffold surface, as visible in Figures 5A and 5B, respectively.

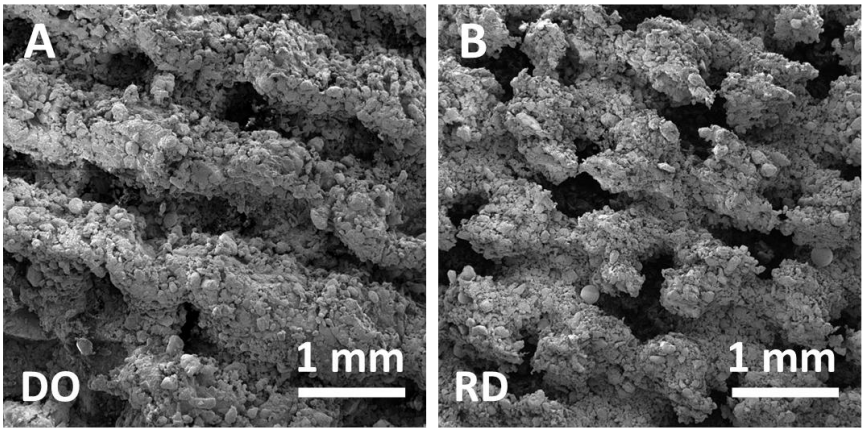


**Figure 5** Micrographs of DO (A) and RD (B) scaffolds surfaces.

After production, to investigate the inner structure, scaffolds with DO and RD geometries were cut at half height. SEM observations (Figure 6A and 6B) show open pores not occluded by powder particles in both geometries.

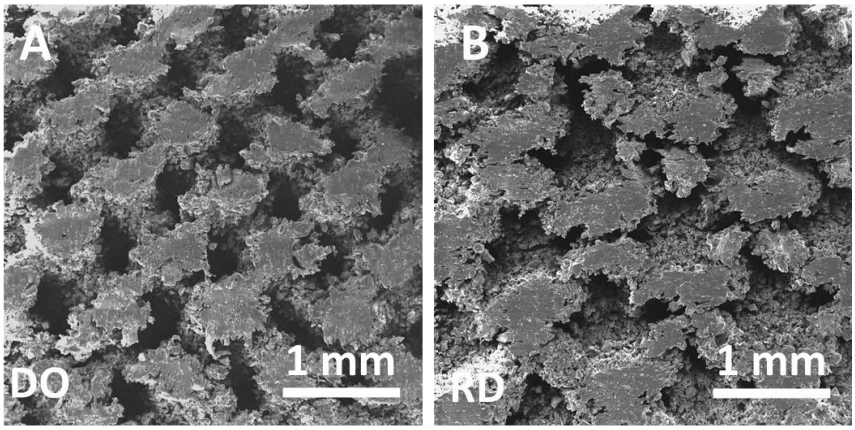


**Figure 6** SEM image of DO (A) and RD (B) inner pores structure.

Amounts of Ca and P (in at.%) obtained by EDS analysis performed on DO and RD scaffolds as well as on raw powder are reported in Table 3. Within experimental uncertainties the Ca/P atomic ratio is the same for raw powder, DO and RD scaffolds, suggesting unchanged stoichiometry of hydroxyapatite in all the analyzed samples. It is worth to note that values of the Ca/P atomic ratio reported in Table 3 for all samples, within experimental error, agree with the nominal value for stoichiometric HA (Ca/P=1.67), as obtained from the HA chemical formula $Ca_{10}(PO_4)_6(OH)_2$.

**Table 3** Results of the EDS chemical analysis for PCL/HA powder, DO and RD scaffolds.

| | **Powder** | **DO** | **RD** |
|---|---|---|---|
| **Ca (at.%)** | 2.7 ± 0.3 | 1.8 ± 0.3 | 2.5 ± 0.5 |
| **P (at.%)** | 1.22 ± 0.13 | 0.90 ± 0.09 | 1.1 ± 0.2 |
| **Ca/P** | 2.2 ± 0.5 | 2.0 ± 0.5 | 2.3 ± 0.9 |

*3.2.2 XRD*

XRD patterns of the scaffold top surface are reported in Figure 7. Patterns of DO (blue line) and RD (red line) geometries are shown in the reduced angular range 2θ = 15° – 45°, where the most intense peaks of both PCL and HA are found. XRD pattern of the mixed raw powder (black line) is also reported in Figure 7 in the same angular range, as reference. PCL peaks are indicated by full dots. Patterns are shifted vertically to ease comparison.

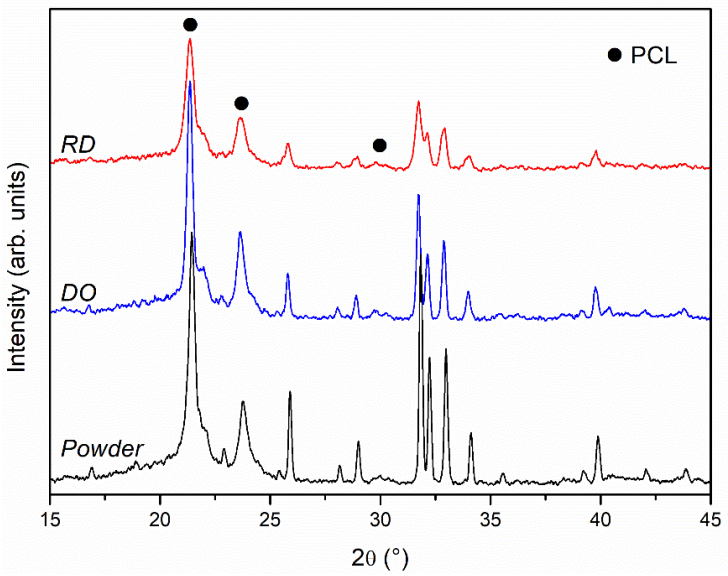


**Figure 7** XRD patterns of the scaffold top surface. Pattern of the mixed raw powder is reported for comparison. PCL – full dots.

Peak shape analysis of XRD patterns provided exact angular position (2θ) and full width at half maximum (FWHM) of most intense peaks. In particular, the two most intense peaks of PCL and the four peaks of HA in the range 2θ = 30 - 35 °C were considered, and results are shown in Table 4. Miller indices (hkl) in Table 4 are reported considering the PCL orthorhombic crystallographic structure proposed by Bittiger et al. [32], while HA structure was taken from ICDD file n. 74-565.

**Table 4** Results of peak shape analysis carried out on most intense XRD peaks of PCL and HA for raw powder and scaffolds with DO and RD elementary unit cell geometry. 2θ - Angular position;

FWHM - Full width at half maximum, hkl - Miller indices. Angular position 2θ and FWHM in degree (°).

| Material | Powder | | Elementary unit cell geometry | | | | hkl |
|---|---|---|---|---|---|---|---|
| | | | DO | | RD | | |
| | *2θ (°)* | *FWHM (°)* | *2θ (°)* | *FWHM (°)* | *2θ (°)* | *FWHM (°)* | |
| **PCL** | 21.445±0.003 | 0.351±0.008 | 21.355±0.001 | 0.282±0.004 | 21.355±0.001 | 0.430±0.005 | (110) |
| | 23.792±0.008 | 0.41±0.03 | 23.658±0.002 | 0.414±0.008 | 23.664±0.003 | 0.51±0.01 | (200) |
| **HA** | 31.836±0.001 | 0.143±0.004 | 31.733±0.001 | 0.175±0.004 | 31.731±0.002 | 0.322±0.007 | (211) |
| | 32.238±0.002 | 0.128±0.007 | 32.141±0.002 | 0.151±0.008 | 32.133±0.004 | 0.21±0.01 | (112) |
| | 32.983±0.002 | 0.155±0.007 | 32.886±0.002 | 0.175±0.006 | 32.878±0.003 | 0.278±0.008 | (300) |
| | 34.115±0.006 | 0.18±0.02 | 33.992±0.007 | 0.24±0.02 | 33.998±0.009 | 0.41±0.03 | (202) |

Comparison of patterns in Figure 7 and results of peak shape analysis in Table 4 clearly shows a general trend to reduced intensity and increased width (FWHM) of diffraction peaks in scaffolds. This suggests a less crystallized structure of both PCL and HA in scaffolds with respect to the raw powder. It is worth to note that this effect is more pronounced in scaffolds with RD unit cell geometry. As for peak angular position, XRD patterns of scaffolds showed a general shift to lower values with respect to raw powder, indicating higher values of lattice parameters of compounds (PCL and HA) in scaffolds (Table 4).

### *3.2.3 Roughness*

Roughness surface maps of DO (Figure 8A) and RD (Figure 8B) scaffolds are shown in Figure 8.

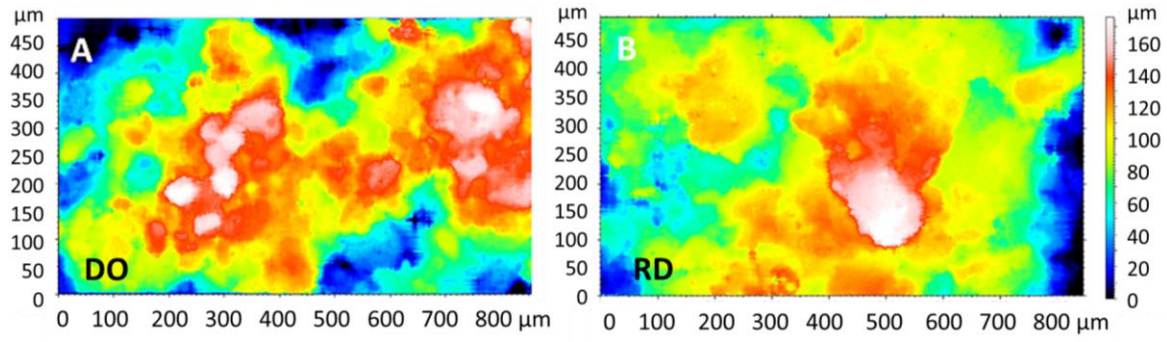


**Figure 8** Roughness surface maps of DO (A) and RD (B) scaffolds.

Parameters connected to surface roughness, calculated from surface maps, are listed in Table 5.

**Table 5** Roughness parameters estimated from the roughness maps.

| | **Parameters** | **DO** | **RD** |
|---|---|---|---|
| **Average surface roughness (Ra) (µm)** | Arithmetic average value of distances in the profile | 31.6 | 30 |
| **Surface skewness (Ssk)** | Symmetry of the profile to the mean line | -0.24 | -0.4 |
| **Surface kurtosis (Sku)** | Sharpness of the profile | 2.4 | 4.28 |
| **Surface peak (Sp) (µm)** | Maximum height from the mean line | 7.8 | 9.3 |
| **Surface valley (Sv) (µm)** | Maximum depth from the mean line | 10 | 11.4 |

Average surface roughness (Ra) is comparable for DO and RD scaffolds. Both geometries present predominance of valleys (Ssk<0), although RD roughness profiles have peak distribution (Sku)

higher and sharper than DO. Moreover, RD has higher values of maximum peak height (Sp) and maximum valley depth (Sv) than DO.

*3.2.4 XμCT*

Scaffolds morphometric parameters obtained by XμCT are listed in Table 6. In our study, scaffold average strut thickness, average micro- and macro-pore size were considered in addition to scaffold volumetric micro-porosity.

**Table 6** Scaffold morphometric parameters obtained by XμCT analysis.

| Parameter | DO | RD |
|---|---|---|
| **Average strut thickness (mm)** | 0.80 ± 0.12 | 0.83 ± 0.13 |
| **Average macro pore size (mm)** | 0.80 ± 0.18 | 1.60 ± 0.18 |
| **Average micro pore size (μm)** | 65 ± 10 | 60 ± 25 |
| **Scaffold micro-porosity (%)** | 8 ± 2% | 8 ± 4% |

The 3D reconstruction of scaffolds in Figure 9, related to 2D slice information, allows to evidence the presence of micro-porosity within DO (Figure 9A) and RD (Figure 9B) struts.

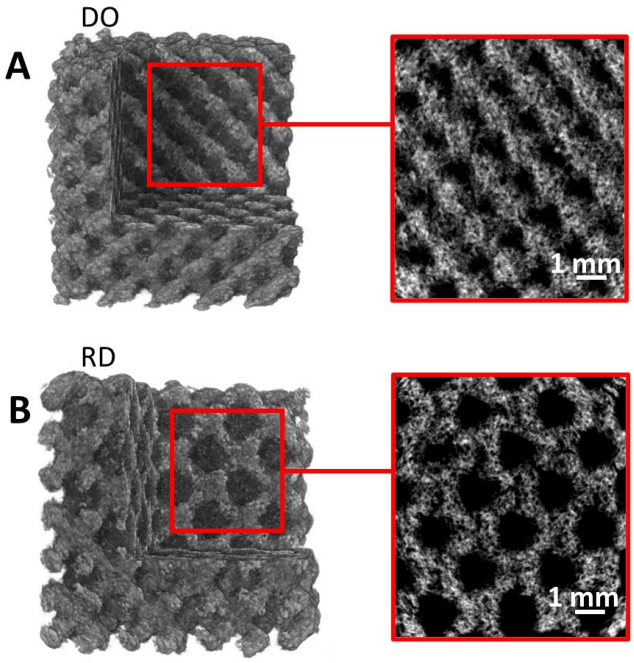


**Figure 9** Micro-porosity inside struts of DO (A) and RD (B) scaffold geometries.

*3.2.5 PhC-XμCT*

The hydroxyapatite volume fraction (vol.%), quantified by PhC-XμCT analysis, is reported in Table 7 for DO and RD scaffolds, after 24 hours cell culture. The HA fraction is about 25 vol.% at the intersection of struts (node) for both DO and RD, while this amount increases of about 10% in the struts that form the macro pores.

**Table 7** – HA volume fraction (vol.%) at the nodes (Node) and in the struts forming the macro pores (Pore) for both DO and RD scaffold geometries after 24 hours cells culture.

| | **DO** | | **RD** | |
|---|---|---|---|---|
| | **Node** | **Pore** | **Node** | **Pore** |
| **HA volume fraction (vol. %)** | 26±5 | 38±6 | 24±5 | 34±2 |

As shown in the 3D reconstructions of VOIs in Figure 10, HA particles (in blue color) accumulate at the macro pores after 24 hours cells incubation, in both DO (Figure 10A) and RD (Figure 10B) scaffolds.

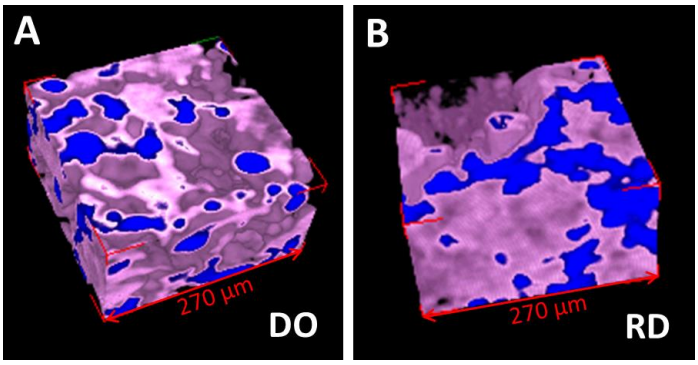


**Figure 10** – 3D model of a VOI after 24 hours cells culture of DO (A) and RD (B) scaffolds. Blue – HA particles; Pink – PCL matrix.

In addition, the specific surface of the material around the macro pores in the DO geometry increases from 24 hours to 4 days cell culture, from 0.079 ± 0.016 $\mu m^{-1}$ to 0.100 ± 0.026 $\mu m^{-1}$. In Figure 11, material erosion after 24 hours (Figure 11A) and 4 days (Figure 11B) cells incubation is compared for the DO geometry. Images clearly show the dispersion of degraded material from struts edge to macro pores.

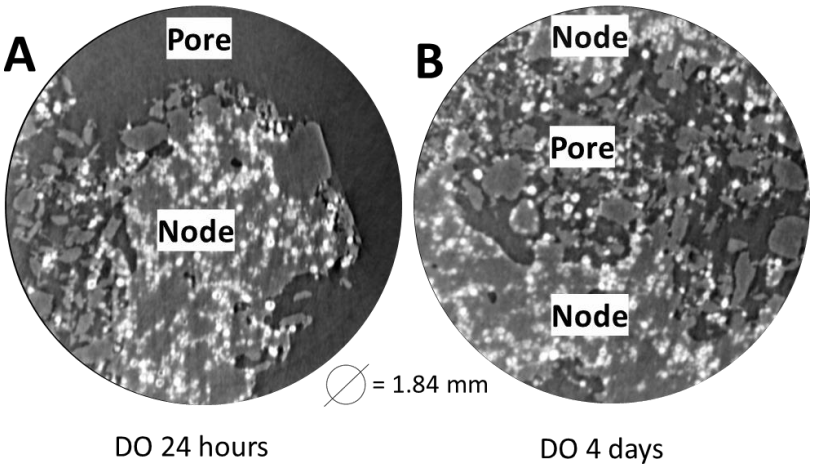


**Figure 11** – Nodes and Pores images obtained by PhC-XµCT reconstruction of DO scaffold after 24 hours (A) and 4 days (B) cells incubation.

*3.3 Mechanical test*

Results of the mechanical tests carried out on DO and RD scaffolds (Figure 12) show similar shape of load/compression curves. Curves exhibit a first steep increase up to about 8% of scaffold height decrease, due to the elastic compression of struts in the elementary unit cell. After elastic deformation (region "Elastic deformation" in Figure 12), the curve shows a slowly increasing linear behavior (region "Plastic collapse" in Figure 12) due to the progressive collapse of struts on compression, followed by an evident increase of the curve slope in coincidence with scaffold compaction (region "Compaction in Figure 12). Compaction of scaffold struts coincides with the upper limit of compression (40%). During the initial steep increase, curves are almost superimposed, suggesting similar mechanical behavior of the two geometries on loading, up to about 70 N. For applied loads above this value, DO exhibits higher ultimate compressive strength respect to RD. For compression values above 10% on initial scaffold height (region "Plastic collapse" in Figure 12), DO requires about 30% higher load value than RD to have the same compression effect. Compaction tests were considered concluded at about 40% of sample height.

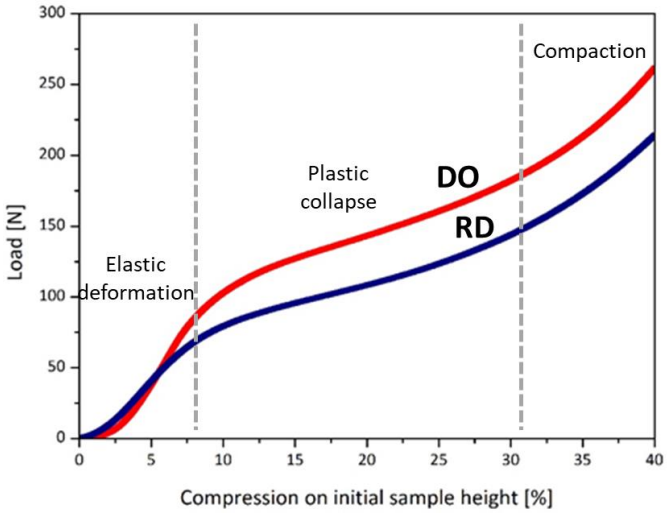


**Figure 12** Results of the compression tests for DO (red curve) and RD (blue curve) scaffolds.

Values of elastic modulus and ultimate compressive strength for DO and RD scaffolds, obtained from mechanical tests in Figure 12 are reported in Table 8, together with the scaffold physical and geometrical characteristics for each specific elementary unit cell geometry (DO and RD). Literature results for PCL/HA scaffolds obtained by LPBF and mandibular bone are also shown in Table 8, for comparison.

**Table 8** Results obtained in this work for DO and RD geometries compared to literature data for PCL/HA (30 wt.%) scaffolds manufactured by LPBF and human mandibular trabecular bone in absence of cortical plates. P – porosity; PS – average pore size; ST – average strut thickness; ρ - relative density; $\rho_s$ – density of strut; E - elastic modulus; $\sigma_{UC}$ – ultimate compressive strength.

| **Reference** | **P (%)** | | **PS (mm)** | | **ST (mm)** | | **ρ** | | **$\rho_s$ (g/cm$^3$)** | | **E (MPa)** | | **$\sigma_{UC}$ (MPa)** | |
|---|---|---|---|---|---|---|---|---|---|---|---|---|---|---|
| **This work** | *DO* | *RD* | *DO* | *RD* | *DO* | *RD* | *DO* | *RD* | *DO* | *RD* | *DO* | *RD* | *DO* | *RD* |
| | 53 | 59 | 0.8 | 1.6 | 0.8 | 0.8 | 0.47 | 0.41 | 0.83 | 0.72 | 15±4 | 13±4 | 2.8±0.5 | 2.6±0.4 |
| **S. Eosoly et al., 2009, 2010, 2012 [10-12]** | 67 | | 1.2 | | 0.6 | | 0.33 | | - | | 1 ÷ 2 | | 0.2 ÷ 0.6 | |
| **S. Eshraghi et al., 2012 [13]** | 81 | | 2 | | 0.7 | | 0.19 | | - | | 36 ± 1 | | 0.9 ± 0.3 | |
| **Human mandibular trabecular bone [33]** | - | | - | | - | | - | | 0.85 ÷ 1.53 | | 3.5 ÷ 125.6 | | 0.22 ÷ 10.44 | |

*3.4 Cell adhesion and proliferation*

Viability tests were performed on DO and RD scaffolds after 24 hours and 4 days hMSCs incubation. In figure 13, data were plotted as percentage of viable cells related to TCPS, set at 100%. Comparative analysis of hMSCs viability at 24 hours and 4 days for both scaffold geometries shows an increase of the average cell viability during the culture period from about 85% to 100% (Figure 13), indicating the material no-cytotoxicity and the ability to support attachment, proliferation and viability of hMSCs. Statistically difference between DO and RD is evident after 4 days incubation with a higher cell viability for RD against DO (* $p < 0.05$). In addition, a statistically significant increase of cell viability is observed in DO from 24 hours to 4 days incubation (Figure 13).

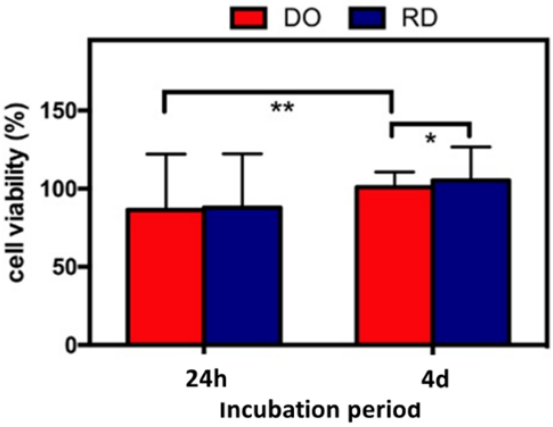


**Figure 13** hMSCS viability after 24 hours (24h) and 4 days (4d) incubation for DO and RD scaffold geometries - * $p < 0.05$; ** $p < 0.01$.

To obtain a clear view of morphology and behavior of the hMSCs, SEM observations were performed after 24 hours incubation (Figure 14) for both DO (Figure 14A) and RD (Figure 14B) scaffolds. As visible in Figure 14, hMSCs spread extensively on the surface of both scaffold type, with noticeable filopodia extensions and cellular protrusions extended across the scaffold pores. It is worth noting that SEM observations after 4 days of culture reveal no hMSCs on either the DO or RD surfaces. This latter effect is most likely due to cellular colonization of the first internal scaffold layers.

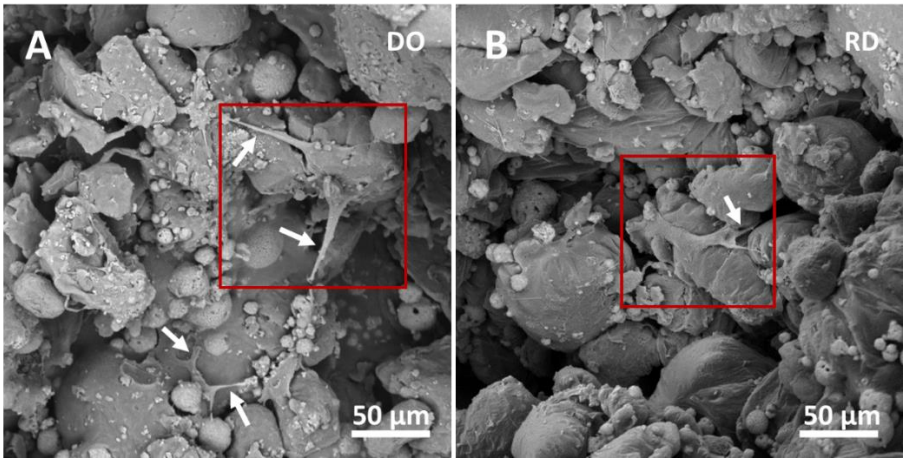


**Figure 14** SEM observations of hMSCs after 24 hours of incubation: DO (A) and RD (B) scaffolds. Single cells in red rectangles; arrows show hMSCs filopodia-like extensions rooted into the pores.

## 4. DISCUSSION

This experimental work takes origin from most suitable literature data matching additive manufacturing technology (LPBF) and material (PCL/HA 30 wt.%), dealing with production and characterization of bioresorbable devices for bone tissue regeneration. Aim of the work is to produce micro- and macro-porous lattice structures to improve mechanical and biological performances of PCL/HA bioresorbable devices.

Two elementary unit cell geometry were considered in this study: a) Diamond (DO) diagonal-symmetrical and b) Rhombic Dodecahedron (RD) midline-symmetrical (Figure 1).

It is worth to note that such combination of elementary unit cell geometry (DO and RD), material (PCL/HA 30 wt.%) and production technology (LPBF), at our best knowledge, has never been studied up to now.

Resorbable scaffolds with macro- and micro-porosity were produced by the LPBF additive manufacturing technology. Macro-porosity was obtained repeating in space the DO and RD elementary unit cells (Figure 1), while micro-porosity, due to the presence of micro-pores inside the struts, was obtained by carefully adjusting the LPBF deposition parameters. The most performing

resorbable scaffolds in terms of mechanical and biological properties were obtained with the deposition parameters reported in Table 2.

The LPBF technology allowed producing resorbable PCL/HA scaffolds with fully interconnected pores, free of residual powder (Figure 6), with total porosity (P) above 50% (Table 8). This porosity value allowed for easy removal of unfused powder by conventional cleaning procedures, thus improving cellular colonization [9].

Topology of the elementary unit cell, regularly repeated in space, determines the macroscopic geometry of scaffold, which is due to the space distribution of macro-pores, and represents a global property. The 3D organization of elementary unit cells defines the geometric arrangement of the material struts in the macro-porous structure (connectivity), and consequently the distribution of macro-porous network (tortuosity). These two quantities (connectivity and tortuosity) influence the mechanical properties of the device and define the resistance to transportation of nutrients and oxygen throughout the macro-pores [34].

Our scaffolds with DO and RD geometries show similar mean strut thickness (Table 6) and porosity (Table 8). Discrepancies between CAD (Table 1) and experimental values of strut thickness (Table 6) and porosity (Table 8) are fully due to the LPBF manufacturing technique.

In the measured value of scaffold porosity is included micro-porosity formed inside struts during the production process. Micro-porosity amounts to about 8%, with average size of micro-pores below 100 μm, independently on unit cell geometry (DO or RD), as estimated by XμCT analysis (Table 6). Micro-porosity was demonstrated to be beneficial to cells penetration [12], due to micro-pores ability to induce capillary forces able to anchor cells to the substrate and deform cells until drawing them into interconnected micro-pores [17].

In quantitative terms, the RD geometry has macro-pores with experimentally estimated average size doubled with respect to DO (Table 6). From this result, it can be concluded that scaffold based on the RD geometry is formed of few large-size macro-pores, while DO shows many small-size macro-pores. Therefore, the RD geometry, which has less connected structures, shows lower tortuosity and

higher porosity than DO. Lower tortuosity and higher porosity are beneficial to the biological response of the scaffold, providing better nutritional pathway to transfer nutrients and molecules to the regions where formation of the new tissue is desired [15].

The elementary unit cell geometry influences scaffold global performances as well as local properties, i.e. not involving the whole scaffold volume. For instance, local heat dissipation during the production process is strongly dependent on scaffold geometry. Tortuosity affects heat dissipation during scaffold fabrication, thus resulting in slower heat dissipation rate for DO (high tortuosity) rather than RD. On the other hand, heat dissipation rate strongly affects material crystallinity during solidification and cooling. Baji et al. [35] have shown that crystallinity, in terms of size and morphology of HA in PCL/HA composites, influences the material properties. In particular, they found that reduction in the size of HA crystals improves resorbability rate in SBF (Simulated Body Fluid) solution and tensile stiffness, suggesting influence of crystallinity on biological and mechanical behavior [35].

In our case, as a measure of crystallinity, full width at half maximum (FWHM) of XRD peaks was adopted, considering that lower FWHM value corresponds to higher crystallinity [36]. XRD results clearly showed that in the mixed raw powder both PCL and HA were crystallized (Figure 3), with the HA phase particularly well crystallized (Table 4), and with the expected HA stoichiometry (Ca/P=1.67), as confirmed, within experimental uncertainties, by EDS analysis (Table 3). On the other hand, XRD analysis carried out on scaffolds showed that crystallinity of PCL and HA depended on unit cell topology (Figure 7 and Table 4), with DO showing higher crystallinity (lower FWHM values) of both phases (PCL and HA) against RD. This latter result confirmed that the higher tortuosity of DO caused slower heat dissipation during scaffold production, resulting in higher crystallinity of phases (PCL and HA), with respect to RD. Although, crystallinity of both PCL and HA depends on scaffold unit cell geometry, residual stresses of the entire scaffold (Figure 7) as well as chemical scaffold composition (Table 3) were independent on geometry (DO or RD).

Heat dissipation rate also affects surface roughness. In DO geometry the heat dissipation rate is low (higher tortuosity), resulting in a longer cooling time which facilitates partial melting of the larger

and denser PCL particles on the scaffold surface (Figure 5). The related consequence of this, is a slightly higher surface roughness of DO than RD (Figure 8 and Table 5).

In addition to SEM images (Figure 2), the large variability in density and size of the PCL particles is confirmed by the thermal behavior on heating of the raw powder. From the PCL powder thermogram in Figure 4 (continuous line), broadening of the endothermic effect proves that the PCL melting process starts at about 40°C, ending around 80°C. This fairly large temperature range that extends over about 40°C is linked to density and size variability of PCL particles. Smaller and less dense powder particles melt at lower temperature, while more dense and larger particles melt at higher temperature, resulting in a melting process of the PCL powder difficult to control during the additive manufacturing process. Thermogram in Figure 4 shows that most of PCL powder particles melt around 70°C, which can be considered as the melting temperature of the PCL powder used in this study.

An additional factor influencing surface roughness is inhomogeneity of the last layer submitted to the laser action during the manufacturing process, due to aggregation of PCL flakes during powder bed feeding and new layer recoating. This latter effect is still active even though the presence of spherically shaped HA particles (Figure 2B) act as solid lubricant by increasing flowability of the raw powder during production. Furthermore, HA does not interfere with the PCL melting process. DSC test performed on HA powder provides a flat curve (Figure 4), indicating absence of any thermal effect in the investigated temperature range, in accordance to literature data [37]. Combination of PCL flakes and HA spherical particles in the blended raw powder allowed obtaining scaffold roughness values of 31.6 μm and 30 μm for DO and RD geometries (Table 5), respectively, that are below the threshold of 56.9 μm above which negative effects on cell growth occur [38]. It is worth to note that values of surface roughness of our scaffolds are similar to those (32±5 μm) reported in literature for cubic lattice scaffolds of PCL/HA (30 wt.%) produced by LPBF [12].

The compressive tests carried out on the two scaffold geometries (DO and RD) show a substantial identical behavior in the elastic regime (same curve shape and elastic modulus value, Figure 12 and

Table 8), where the elastic properties of the material as well as the elementary unit cell geometry mainly control the mechanical response. In the elastic region, the geometry contribution is due to the elastic response of struts, where pores are not yet flattened and broken, as gradually occurs during plastic collapse [10,14]. Similar values of strut thickness (ST) and relative density ($\rho$) in Table 8 for DO and RD geometries confirms this mechanism.

In the region of plastic deformation (Figure 12) struts of the elementary unit cells progressively collapse under the applied load. In this region, DO requires 30% higher load to reach the same compaction value of RD (Figure 12). This effect is due to smaller macro-pores of DO than RD (Table 8) at constant strut thickness, resulting in a more connected and space-opened channels. Therefore, the elementary unit cell geometry (connectivity and tortuosity) mainly governs the mechanical behavior during the plastic collapse of scaffold.

Collapse of the scaffold structure continues up to compaction, where the compressive curve shows similar behavior for the two geometries (DO and RD). Values of ultimate compressive strength in Table 8 are equal, within experimental uncertainties, independently on elementary unit cell geometry. This latter result shows that, at compaction, when the whole scaffold structure is collapsed and pores flattened, the mechanical response mainly depends on material properties.

Therefore, from the mechanical behavior of scaffolds three different regimes can be inferred: a) elastic deformation, controlled by material properties and elementary unit cell geometry, b) plastic deformation, controlled by elementary unit cell geometry and c) compaction, depending on material. Considering that the density of struts ($\rho_s$) of our scaffolds is in the range of human mandibular trabecular bone (Table 8), comparison of mechanical performances of scaffolds to native bone is allowed. The mechanical parameter considered in this case is the ultimate compressive strength (Table 8). Experimental results clearly show that both DO, and RD scaffolds geometries perfectly match with the range of values of the ultimate compressive strength of middle region of human mandibular trabecular bone in absence of cortical plates [33]. Therefore, from a mechanical point of view, our scaffolds are suitable for human mandibular bone tissue regeneration.

Since the elastic behavior of scaffold is governed by both material response and unit cell geometry, values of the elastic modulus of our scaffolds (Table 8) are different to the values reported in literature, because of the different geometries studied.

However, independently on unit cell geometry (DO or RD), our scaffolds always show higher resistance to compression (ultimate compressive strength $\sigma_{UC}$ in Table 8) than cubic lattice structure by S. Eosoly et al. [10-12] and scaffold with orthogonal porous square channels by S. Eshraghi et al. [13].

Biological performances of scaffolds, tested with short-term hMSCs viability, consist of DO and RD ability to provide a support for cell adhesion and proliferation (Figure 13). Furthermore, DO and RD scaffold geometries allow cell migration from surface (Figure 14) to the inner scaffold layers, as confirmed by absence of hMSCs detected by SEM on the top surface of DO and RD scaffolds after 4 days of incubation. In particular, the hMSCs viability trend is greater in RD scaffold geometry with respect to DO, due to higher pores size and porosity and lower connectivity and tortuosity, which make cells able to colonize the whole structure with the appropriate supply of nutrients and oxygen.

Under physiological conditions of cell culture, three factors mainly influence PCL degradation: a) geometrical features of the sample, b) PCL raw powder molecular weight and c) local environment characteristics as fluid flow, temperature, and pH [39,40]. An additional factor reported in literature, capable of affecting PCL degradation, is incorporation of ceramic compounds such as hydroxyapatite [40]. In the present study, all these effects are present and cooperate to the scaffold degradation. High porosity level and large pores size (Table 6) enable fluid infiltration into the structure [40]. In addition, scaffold micro porosity within struts (Figure 9A and 9B) is a factor that accelerates the material degradative process, allowing fluid infiltration also inside the struts [41]. Variability of the PCL molecular weight in the raw powder (Figure 4), allowed more likely the release of short chains by the bulk, anticipating mass loss from the matrix [40]. Local environment is characterized by the cells incubation conditions and DMEM flow, affected by scaffold tortuosity. According to Bartnikowski et al. [40], in physiological conditions, degradation appears more rapid *in vivo* then *in vitro*.

Furthermore, they also reported that in the *in vitro* environment, degradation is faster in the presence of cells (cell-containing environment) than in the absence of cells (cell-free environment) [40]. Giuliani et al. [42] showed that cells accelerate the resorption time of scaffold compared to the biopolymer spontaneous hydrolysis, that occurs during culture as a consequence of the PCL hydrophobicity. Studies have already demonstrated the interaction between cellular microenvironment and biomaterial. Eosoly et al. [12] observed changes in microarchitecture of struts after 1 week of incubation of PCL/HA scaffold with MC 3T3 mouse calvarial osteoblast cells, while Yeong et al. [9] observed similar effects after 6 days of C2C12 myoblast cells culture on PCL scaffold. Furthermore, addition of HA particles accelerates the degradation of PCL, due to preferred attack at the ceramic/polymer interface by water with consequent weight loss, followed by macroscopic structural breakdown and small polymer fragments metabolized by cells [43]. Reis et al. [44] found that the dispersion of HA quantities up to 30 wt.%, tend to increase the degradation rate in a simulated physiological solution, while, as already mentioned above, the same effect was observed by Baji et al. [35] on reducing the size of HA crystals.

PhC-XμCT results on our scaffolds after 24 hours of incubation, evidenced PCL degradation in scaffolds due to the combined effects of elementary unit cell geometry, PCL molecular weight, culture medium, presence of cells, as well as amount and size of crystalline HA. In fact, after hMSCs adhesion (24h), the HA content is higher near the macro pores than in the node (Table 7). Figure 10 confirms this trend, showing that after 24 hours of culture, near the pores, the HA concentration increases because of the PCL degradation. Further confirmation of the interaction between stem cells and biomaterial is the strong increase of material specific surface in the scaffold nodes, from 24 hours to 4 days of culture. This increase is due to material disintegration with the resulting pores filled with the eroded material from struts around the macro-pores, as illustrated in Figure 11.

In conclusion, results of this experimental work clearly show that scaffold design tailored with DO and RD elementary unit cells geometry, produced by the LPBF technology with appropriate machining parameters for micro- and macro-porosity, allow to meet the mechanical requirements of

human mandibular trabecular bone and the short-term needs for adhesion, proliferation and migration of hMSCs. Furthermore, the combination of elementary cell geometry, blended raw powder and cell culture conditions improves the biodegradable response of the scaffolds by accelerating the degradation rate of PCL compared to similar studies. [9,12].

## 5. CONCLUSIONS

This experimental study tried to fill gap in literature on resorbable lattice scaffold in PCL/HA (30 wt.%) produced by LPBF for bone tissue regeneration. Micro- and macro- porous scaffolds were obtained by the repetition of Diamond (DO) and Rhombic Dodecahedron (RD) elementary unit cells. Structural, mechanical, and biological characterizations were carried out on scaffolds to investigate the biomechanical behavior of each elementary unit cell geometry (DO and RD) in perspective of bone tissue regeneration.

Experimental results clearly showed that both geometries (DO and RD), in terms of biomechanical response and bioresorbability, are suitable for human mandibular trabecular bone regeneration.

The main results obtained in this study can be summarized as follows:

- In the blended raw powder as well as in the scaffolds, PCL and HA are crystallized and stoichiometric;
- Scaffold total porosity (micro and macro) is higher than 50% for the investigated geometries (DO and RD), with micro-porosity amounting to about 8% in the two cases;
- Different geometry of the elementary unit cell reflects on connectivity and tortuosity of macro-pores in the scaffolds. The RD geometry shows lower tortuosity with larger macro-pores than DO;
- Surface roughness of scaffolds is influenced from the thermal behavior on heating of PCL and HA. Heat dissipation rate during cooling mainly depends on scaffold tortuosity, thus resulting in higher surface roughness value for DO than RD;
- Mechanical response of scaffolds submitted to compressive tests evidenced three distinct regions: a) the elastic regime governed by elementary unit cell geometry and material properties, b)

the plastic deformation behavior due to the macroscopic geometrical properties (connectivity and tortuosity) of scaffolds, and c) the compaction region where the material properties determine the mechanical response;

- The ultimate compressive strength values of both DO and RD geometries match with the range of values of the middle region of human mandibular trabecular bone in absence of cortical plates;
- Although the biological response is acceptable for both geometries (DO and RD), RD provides a better 3D environment for hMSCs adhesion and proliferation for scaffold colonization;
- The presence of micro-pores within the struts enhances the scaffold degradation.

Results obtained in this study evidenced the suitability of PCL/HA (30 wt.%) resorbable lattice scaffolds with DO and RD elementary unit cell geometry as temporary supports for bone tissue regeneration. Appropriate combination of PCL/HA with the Laser Powder Bed Fusion (LPBF) technology, which can produce patient customized resorbable scaffolds, opens very important perspectives in the fields of bone regeneration and tissue engineering.

## ACKNOWLEDGEMENTS

This study was conducted under the collaboration with Prosilas - Rapid Prototyping, Via Terracini 14 – zona Industriale A, 60212 Civitanova Marche (MC) – Italia and a grant of the Italian Ministry of Education, University and Research (MIUR) to the Department of Molecular Medicine of the University of Pavia under the initiative “Dipartimenti di Eccellenza (2018–2022)”.

## REFERENCES

[1] Prakasam, M., Locs, J., Salma-Ancane, K., Loca, D., Largeteau, A., & Berzina-Cimdina, L. (2017). Biodegradable Materials and Metallic Implants—A Review. Journal of Functional Biomaterials, 8(4), 44. https://doi.org/10.3390/jfb8040044

[2] Prasad, A. (2021). State of art review on bioabsorbable polymeric scaffolds for bone tissue engineering. Materials Today: Proceedings, S2214785320392968. https://doi.org/10.1016/j.matpr.2020.11.622

[3] Iqbal, N., Khan, A. S., Asif, A., Yar, M., Haycock, J. W., & Rehman, I. U. (2019). Recent concepts in biodegradable polymers for tissue engineering paradigms: A critical review. International Materials Reviews, 64(2), 91–126. https://doi.org/10.1080/09506608.2018.1460943

[4] Asghari, F., Samiei, M., Adibkia, K., Akbarzadeh, A., & Davaran, S. (2017). Biodegradable and biocompatible polymers for tissue engineering application: A review. Artificial Cells, Nanomedicine, and Biotechnology, 45(2), 185–192. https://doi.org/10.3109/21691401.2016.1146731

[5] Lett, J.A., Sagadevan, S., Fatimah, I., Hoque, M. E., Lokanathan, Y., Léonard, E., Alshahateet, S. F., Schirhagl, R., & Oh, W. C. (2021). Recent advances in natural polymer-based hydroxyapatite scaffolds: Properties and applications. European Polymer Journal, 148, 110360. https://doi.org/10.1016/j.eurpolymj.2021.110360

[6] Szymczyk-Ziółkowska, P., Łabowska, M. B., Detyna, J., Michalak, I., & Gruber, P. (2020). A review of fabrication polymer scaffolds for biomedical applications using additive manufacturing techniques. Biocybernetics and Biomedical Engineering, 40(2), 624–638. https://doi.org/10.1016/j.bbe.2020.01.015

[7] Alizadeh-Osgouei, M., Li, Y., & Wen, C. (2019). A comprehensive review of biodegradable synthetic polymer-ceramic composites and their manufacture for biomedical applications. Bioactive Materials, 4, 22–36. https://doi.org/10.1016/j.bioactmat.2018.11.003

[8] Kudelski, R., Cieslik, J., Kulpa, M., Dudek, P., Zagorski, K., Rumin, R. Comparison of Cost, Material and Time Usage in FDM and SLS 3D Printing Methods, MEMSTECH 2017, 20-23 April, 2017, Polyana-Svalyava (Zakarpattya), UKRAINE.

[9] Yeong, W.Y., Sudarmadji, N., Yu, H.Y., Chua, C.K., Leong, K.F., Venkatraman, S.S., Boey, Y.C.F., & Tan, L.P. (2010). Porous polycaprolactone scaffold for cardiac tissue engineering

fabricated by selective laser sintering. Acta Biomaterialia, 6(6), 2028–2034. https://doi.org/10.1016/j.actbio.2009.12.033

[10] Eosoly, S., Lohfeld, S., Brabazon, D. Effect of hydroxyapatite on biodegradable scaffolds fabricated by SLS, Key Engineering Materials Vols 396-398 (2009) pp 659-662. doi:10.4028/www.scientific.net/KEM.396-398.659.

[11] Eosoly, S., Brabazon, D., Lohfeld, S., Looney, L. Selective laser sintering of hydroxyapatite/poly-e-caprolactone scaffolds, Acta Biomaterialia 6 (2010) 2511–2517. doi:10.1016/j.actbio.2009.07.018.

[12] Eosoly, S., Vrana, N.E., Lohfeld, S., Hindie, M., Looney, L. Interaction of cell culture with composition effects on the mechanical properties of polycaprolactone-hydroxyapatite scaffolds fabricated via selective laser sintering (SLS), Materials Science and Engineering C 32 (2012) 2250–2257. doi:10.1016/j.msec.2012.06.011.

[13] Eshraghi S. and Das S., Micromechanical finite-element modeling and experimental characterization of the compressive mechanical properties of polycaprolactone–hydroxyapatite composite scaffolds prepared by selective laser sintering for bone tissue engineering, Acta Biomaterialia 8 (2012) 3138–3143. http://dx.doi.org/10.1016/j.actbio.2012.04.022.

[14] Wiria, F.E., Leong, K.F., Chua, C.K., Liu, Y. Poly-e-caprolactone/hydroxyapatite for tissue engineering scaffold fabrication via selective laser sintering, Acta Biomaterialia 3 (2007) 1–12. doi:10.1016/j.actbio.2006.07.008.

[15] Li, J., Chen, D., Fan, Y., Evaluation and Prediction of Mass Transport Properties for Porous Implant with Different Unit Cells: A Numerical Study, BioMed Research International Volume 2019, Article ID 3610785, 11 pages. https://doi.org/10.1155/2019/3610785.

[16] Li, J., Chen, D., Zhang, Y., Yao, Y., Mo, Z., Wang, L., Fan, Y., Diagonal-symmetrical and Midline-symmetrical Unit Cells with Same Porosity for Bone Implant: Mechanical Properties Evaluation, J. Bionic. Eng. 16 (2019) 468–479. https://doi.org/10.1007/s42235-019-0038-z.

[17] Zhang, K., Fan, Y., Dunne, N., & Li, X. (2018). Effect of microporosity on scaffolds for bone tissue engineering. Regenerative Biomaterials, 5(2), 115–124. https://doi.org/10.1093/rb/rby001

[18] Abbasi, N., Hamlet, S., Love, R. M., & Nguyen, N.-T. (2020). Porous scaffolds for bone regeneration. Journal of Science: Advanced Materials and Devices, 5(1), 1–9. https://doi.org/10.1016/j.jsamd.2020.01.007

[19] Giuliani, A., Gatto, M.L., Gobbi, L., Mangano, F.G., Mangano, C. Integrated 3D Information for Custom-Made Bone Grafts: Focus on Biphasic Calcium Phosphate Bone Substitute Biomaterials. International Journal of Environmental Research and Public Health 2020, 17(14), 4931. https://doi.org/10.3390/ijerph17144931.

[20] Siddiqui, N., Asawa, S., Birru, B., Baadhe, R., Rao, S. PCL-Based Composite Scaffold Matrices for Tissue Engineering Applications, Molecular Biotechnology (2018) 60:506–532. https://doi.org/10.1007/s12033-018-0084-5.

[21] Hajiali, F., Tajbakhsh, S., Shojaei, A. Fabrication and Properties of Polycaprolactone Composites Containing Calcium Phosphate-Based Ceramics and Bioactive Glasses in Bone Tissue Engineering: A Review, Polymer Reviews, 58:1, 164-207. DOI:10.1080/15583724.2017.1332640.

[22] Heo, S.-J., Kim, S.-E., Wei, J., Hyun, Y.-T., Yun, H.-S., Kim, D.-H., Shin, J.W., Shin, J.-W. Fabrication and characterization of novel nano- and micro-HA/PCL composite scaffolds using a modified rapid prototyping process, Journal of Biomedical Materials Research Part A (20018). https://doi.org/10.1002/jbm.a.31726.

[23] Balu, R., Kumar, T.S. S., Ramalingam, M., & Ramakrishna, S. (2011). Electrospun Polycaprolactone/Poly(1,4-butylene adipate-co-polycaprolactam) Blends: Potential Biodegradable Scaffold for Bone Tissue Regeneration. Journal of Biomaterials and Tissue Engineering, 1(1), 30–39. https://doi.org/10.1166/jbt.2011.1004

[24] Gatto, M.L., Groppo, R., Bloise, N., Fassina, L., Visai, L., Galati, M., Iuliano, L., Mengucci, P., Topological, Mechanical and Biological Properties of Ti6Al4V Scaffolds for Bone Tissue

Regeneration Fabricated with Reused Powders via Electron Beam Melting. Materials 2021, 14, 224. https:// doi.org/10.3390/ma14010224

[25] Brun, F., Massimi, L., Fratini, M., Dreossi, D., Billé, F., Accardo, A., Pugliese, R., Cedola, A., SYRMEP Tomo Project: a graphical user interface for customizing CT reconstruction workflows, Adv Struct Chem Imaging 3(1):4, 2017.

[26] Paganin, D., Mayo, S.C., Gureyev, T.E., Miller, P.R., Wilkins, S.W. Simultaneous phase and amplitude extraction from a single defocused image of a homogeneous object, J Microsc. 206 (Pt 1):33–40, 2002.

[27] Schneider, C.A., Rasband, W.S., Eliceiri, K.W. NIH Image to ImageJ: 25 years of image analysis, Nat. Methods 9(7) 671–5, 2012.

[28] ISO 25178-603:2013, Geometrical Product Specifications (GPS) - Surface Texture: Areal - Part 603: Nominal Characteristics of Non-Contact (Phase-Shifting Interferometric Microscopy) Instruments, International Organization for Standardization, Geneva, Switzerland 2013

[29] ASTM D 1621e10, Standard Test Method for Compressive Properties of Rigid Cellular Plastics

[30] Bernardo, M.E., Avanzini, M.A., Perotti, C., Cometa, A.M., Moretta, A., Lenta, E., Del Fante, C., Novara, F., de Silvestri, A., Amendola, G., Zuffardi, O., Maccario, R., Locatelli, F. Optimization of in vitro expansion of human multipotent mesenchymal stromal cells for cell-therapy approaches: further insights in the search for a fetal calf serum substitute, Cell Physiol. 2007, 211, 121-30. https://doi.org/10.1002/jcp.20911.

[31] Ceccarelli, G., Bloise, N., Mantelli, M., Gastaldi, G., Fassina, L., De Angelis, M.G.C., Ferrari, D., Imbriani, M., Visai, L. A Comparative Analysis of the In Vitro Effects of Pulsed Electromagnetic Field Treatment on Osteogenic Differentiation of Two Different Mesenchymal Cell Lineages, Biores. Open Access. 2013, 2, 283–294. https://doi.org/10.1089/biores.2013.0016.

[32] Bittiger, H., Marchessault, R.H., & Niegisch, W.D. (1970). Crystal structure of poly-ε-caprolactone. Acta Crystallographica Section B: Structural Crystallography and Crystal Chemistry, 26(12), 1923-1927.

[33] Misch, C.E., Qu, Z., Bidez, M.W. Mechanical Properties of Trabecular Bone in the Human Mandible: Implications for Dental Implant Treatment Planning and Surgical Placement, J Oral Maxiilofac Surg 57:700-706, 1999.

[34] Starly, B., Yildirim, E., & Sun, W. (2007). A tracer metric numerical model for predicting tortuosity factors in three-dimensional porous tissue scaffolds. Computer Methods and Programs in Biomedicine, 87(1), 21–27. https://doi.org/10.1016/j.cmpb.2007.04.003

[35] Baji, A., Wong, S. C., Liu, T., Li, T., & Srivatsan, T. S. (2007). Morphological and X-ray diffraction studies of crystalline hydroxyapatite-reinforced polycaprolactone. Journal of Biomedical Materials Research Part B: Applied Biomaterials: An Official Journal of The Society for Biomaterials, The Japanese Society for Biomaterials, and The Australian Society for Biomaterials and the Korean Society for Biomaterials, 81(2), 343-350

[36] Cullity, B.D., S:R: Stock, "Elements of X-Ray Diffraction", Third Edition, Pearson New International Edition (2014).

[37] Suchanek, W., Yashima, M.; M. Kakihana, M. Yoshimura, Hydroxyapatite ceramics with selected sintering additives, Biomoterials 18 (1997) 923-933.

[38] Trevisan F., Calignano F., Aversa A., Marchese G., Lombardi M., Biamino S., Ugues D., Manfredi D., Additive manufacturing of titanium alloys in the biomedical field: processes, properties and applications, Journal of Applied Biomaterials & Functional Materials 2018, Vol. 16(2) 57–67. https://doi.org/10.5301/jabfm.5000371.

[39] Bloise, N., Patrucco, A., Bruni, G., Montagna, G., Caringella, R., Fassina, L., Tonin, C., Visai, L. In Vitro Production of Calcified Bone Matrix onto Wool Keratin Scaffolds via Osteogenic Factors and Electromagnetic Stimulus. Materials (Basel). 2020 Jul 8;13(14):3052. doi: 10.3390/ma13143052. PMID: 32650489; PMCID: PMC7411850.

[40] Bartnikowski, M., Dargaville, T.R., Ivanovski, S., & Hutmacher, D.W. (2019). Degradation mechanisms of polycaprolactone in the context of chemistry, geometry and environment. Progress in Polymer Science, 96, 1–20. https://doi.org/10.1016/j.progpolymsci.2019.05.004

[41] Visscher, L.E., Dang, H.P., Knackstedt, M.A., Hutmacher, D.W., & Tran, P.A. (2018). 3D printed Polycaprolactone scaffolds with dual macro-microporosity for applications in local delivery of antibiotics. Materials Science and Engineering: C, 87, 78–89. https://doi.org/10.1016/j.msec.2018.02.008

[42] Giuliani, A., Moroncini, F., Mazzoni, S., Belicchi, M.L. C., Villa, C., Erratico, S., Colombo, E., Calcaterra, F., Brambilla, L., Torrente, Y., Albertini, G., Della Bella, S. Polyglycolic Acid–Polylactic Acid Scaffold Response to Different Progenitor Cell In Vitro Cultures: A Demonstrative and Comparative X-Ray Synchrotron Radiation Phase-Contrast Microtomography Study. Tissue Eng. Part C Methods 2014, 20 (4), 308–316. https://doi.org/10.1089/ten.tec.2013.0213.

[43] Azevedo, M.C., Reis, R.L., Claase, M.B., Grijpma, D.W., & Feijen, J. (s.d.). Development and properties of polycaprolactone/hydroxyapatite composite biomaterials. 5.

[44] Reis, R.L., Cuhna, M., Bevis, M.J. (1997). Using Nonconventional Processing to Develop Anisotropic and Biodegradable Composites of Starch-Based Thermoplastics Reinfored with Bone-Like Ceramics. Medical Plastics and Biometerials, 46, 4.